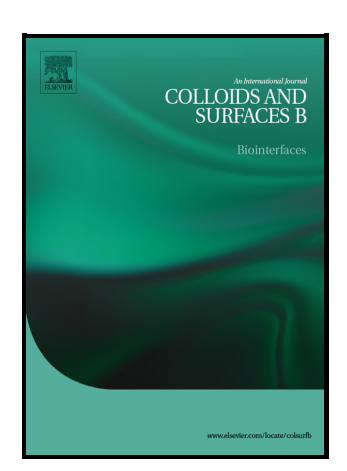
Journal Pre-proof

Electrospun Nanofibrous Scaffolds Reinforced with Therapeutic Lithium/Manganese-Doped Calcium Phosphates: Advancing Skin Cancer Therapy through Apoptosis Induction

Sara Gorgani, Farzad Kermani, Khatereh Sadeghzadeh, Arghavan Vojdani, Sara Hooshmand, Kobra Foroughi, Zoleikha Azari, Seyede Atefe Hosseini, Sahar Mollazadeh, Alireza Ebrahimzadeh Bideskan, Simin Nazarnezhad



PII: S0927-7765(24)00607-6

DOI: https://doi.org/10.1016/j.colsurfb.2024.114348

Reference: COLSUB114348

To appear in: Colloids and Surfaces B: Biointerfaces

Received date: 27 September 2024 Revised date: 29 October 2024 Accepted date: 30 October 2024

Please cite this article as: Sara Gorgani, Farzad Kermani, Khatereh Sadeghzadeh, Arghavan Vojdani, Sara Hooshmand, Kobra Foroughi, Zoleikha Azari, Seyede Atefe Hosseini, Sahar Mollazadeh, Alireza Ebrahimzadeh Bideskan and Simin Nazarnezhad, Electrospun Nanofibrous Scaffolds Reinforced with Therapeutic Lithium/Manganese-Doped Calcium Phosphates: Advancing Skin Cancer Therapy through Apoptosis Induction, *Colloids and Surfaces B: Biointerfaces*, (2024) doi:https://doi.org/10.1016/j.colsurfb.2024.114348

This is a PDF file of an article that has undergone enhancements after acceptance, such as the addition of a cover page and metadata, and formatting for readability, but it is not yet the definitive version of record. This version will undergo additional copyediting, typesetting and review before it is published in its final form, but we are providing this version to give early visibility of the article. Please note that, during the production process, errors may be discovered which could affect the content, and all legal disclaimers that apply to the journal pertain.

Electrospun Nanofibrous Scaffolds Reinforced with Therapeutic Lithium/Manganese-

Doped Calcium Phosphates: Advancing Skin Cancer Therapy through Apoptosis Induction

Sara Gorgani^a, Farzad Kermani^a, Khatereh Sadeghzadeh^b, Arghavan Vojdani^c, Sara Hooshmand^{d,*}, Kobra Foroughi^b, Zoleikha Azari^b, Seyede Atefe Hosseini^{c,f}, Sahar Mollazadeh^c, Alireza Ebrahimzadeh Bideskan^{b,g,*}, Simin Nazarnezhad^{h,a,*}

^aTissue Engineering Research Group (TERG), Department of Anatomy and Cell Biology, School of Medicine, Mashhad University of Medical Sciences, Mashhad 917794-8564, Iran

^bDepartment of Anatomy and Cell Biology, School of Medicine, Mashhad University of Medical Sciences, Mashhad 917794-8564, Iran

^cDepartment of Materials Engineering, Faculty of Engineering, Ferdowsi University of Mashhad (FUM), Azadi Sq., Mashhad 917794-8564, Iran

^dDepartment of Biological and Chemical Engineering, Aarhus University, Aarhus, Denmark

^eDepartment of Medical Biotechnology and Nanotechnology, Faculty of Medicine, Mashhad University of Medical Sciences, Mashhad, Iran

^fBiological Sciences (IZN), Buchman Institute for Molecular Life Sciences (BMLS), Goethe-Universität Frankfurt am Main, Germany

^gApplied Biomedical Research Center, School of Medicine, Mashhad University of Medical Sciences, Mashhad, Iran

^hMetabolic Syndrome Research Center, Mashhad University of Medical Sciences, Mashhad, Iran

Correspondence:

Sara Hooshmand (sarah@bce.au.dk),

Alireza Ebrahimzadeh Bideskan (ebrahimzadehba@mums.ac.ir),

Simin Nazarnezhad (nazarnezhads@mums.ac.ir)

Abstract

In the current study we fabricated potent materials by incorporating therapeutic elements into

calcium phosphates (CPs) to combat cancer. This involved synthesizing manganese (Mn)- and

lithium (Li)-doped CPs and loading them into electrospun nanofibers (NFs) composed of chitosan

(CS) and polyethylene oxide (PEO). The characterized CPs exhibited excellent properties,

including a particle size of 47-75 nm, surface charge of –(30-56) mV, and specific surface area of

75-266 m²/g. The electrochemical analysis revealed that Mn and Mn/Li-doped CPs are promising

for generating oxygen free radicals and H₂O₂, crucial for cancer therapy. Biological evaluation

showcased the outstanding performance of the developed materials. MTT assay revealed a

cytotoxic effect of nano-constructs on melanoma A375 cell line without adverse effects on normal

L929 cells over 72 h. Annexin V/PI apoptosis assay indicated substantial apoptosis rates in A375

cells treated with PC-20% (62.55 \pm 4.59%). The obtained data of qPCR analysis of pro-apoptotic

and anti-apoptotic genes (P53, Bax, Bcl-2) in A375 cells treated with different CP nanoparticles

(NPs) showed a significant increase in P53 and Bax gene expression, indicating high levels of

A375 cell apoptosis. Additionally, the samples containing Mn ion exhibited high reactive oxygen

species (ROS) generation. In conclusion, the fabricated NFs scaffolds hold promising potential for

cancer therapy.

Keywords: Calcium phosphate, Electrospun nanofiber, Skin Tissue Engineering, Skin cancer

2

1. Introduction

Despite extensive efforts, cancer has remained the second leading cause of death globally [1, 2]. Melanoma constitutes 1.7% of global cancer cases, with an estimated 57,000 deaths attributed to melanoma in 2020, as reported by GLOBOCAN [3, 4]. In this condition, excessive proliferation of melanocytes in the epidermis can be resulted from various gene mutations [5]. Although conventional therapeutic modalities (e.g., surgical excision, chemotherapy, radiotherapy, or combination therapy) are applicable in primary stages, their efficacy is often compromised by tumor recurrence due to metastasis or regrowth of residual tumor cells [6].

Recent advancements in nanotechnology have demonstrated promising outcomes for treating various cancer types, particularly melanoma [5, 6]. It is worth noting that nanosystem platforms can enable the direct delivery of substantial amounts of therapeutics to the tumor site, enhancing their therapeutic efficacy. Utilizing nanoparticles (NPs) and nanofibers (NFs), either alone or in conjunction with drug substances, has garnered significant attention owing to their facile transport, potential for specific cell targeting, sustained release, and improved therapeutic outcomes [5, 7]. Calcium phosphates (CP), which are composed of primary minerals within the human body, have found extensive applications in various facets of tissue engineering [8-10]. In the realm of cancer research, researchers have exploited diverse forms of CPs as carriers. Among these, hydroxyapatite (HAp), β-tricalcium phosphate (β-TCP), dicalcium phosphate dihydrate (DCPD), and dicalcium phosphate anhydrate (DCPA) have been emerged as pivotal subcategories with notable anti-cancer effects [11, 12]. The utilization of these CPs, either independently or as vehicles of anti-cancer materials, has garnered significant attention in the realms of cancer diagnosis and therapy [11]. Various chemotherapeutic agents have been effectively loaded into these CP formulations, undergoing thorough evaluations of their drug delivery capacities. Not only limited to

pharmaceuticals but also the strategic incorporation of distinct elements with specific biological properties into the chemical structure of CPs can be an efficacious approach for enhancing or introducing specific attributes to the ultimately synthesized compositions [13, 14]. In the realm of cancer research, the substitution of elements such as europium (Eu), ferrous (Fe), manganese (Mn), and neodymium (Nd) are successful examples where these elements have been integrated into the CPs' structure [15-17]. This integration has yielded particles endowed with robust luminescent effects suitable for imaging, as well as thermal, magnetic, and near-infrared (NIR) fluorescence capabilities for applications in photothermal therapies. Furthermore, the inclusion of certain radioisotopes (e.g., strontium, phosphorus, and gadolinium) can establish an internal source for beta and gamma radiation, addressing the eradication of cancer tumors [18-22].

The utilization of tumor-specific therapies has gained significant attention in cancer treatment, aiming to mitigate the adverse effects associated with conventional approaches. Chemodynamic therapy represents an ongoing treatment strategy wherein hydrogen peroxide (H₂O₂) within the tumor microenvironment (TME) is harnessed to generate the potent reactive oxygen species (ROS) known as hydroxyl radicals (·OH) through Fenton/Fenton-like reactions, targeting tumor cells [23, 24]. Notably, extensive research endeavors involve the incorporation of transition metal ions (e.g., Fe, Mn, copper, nickel) to instigate Fenton/Fenton-like reactions within the TME [25]. Additionally, a growing body of evidence suggests the potential anti-metastatic role of lithium (Li) in primary colon cancer models during tumorigenesis [26, 27].

The utilization of NF scaffolds as carriers is a prevalent approach in the biomedical domain for drug delivery, facilitating sustained release within tumor sites [28]. Electrospinning stands out as a widely adopted technique for the mass production of NFs. Variations in polymer selection and

adjustments to electrospinning parameters, such as nozzle-collector distance, voltage, and spinning rate can lead to the fabrication of NFs with diverse diameters and arrangements [29].

Administration of chitosan (CS) has a long history in biomedical field since it possesses a wide range of biological effects; e.g., anti-inflammatory, anti-microbial, anti-fungal, anti-hyperglycemic, and anti-oxidant effects [28, 30-34]. Nevertheless, the intrinsic limitations such as elevated viscosity, brittleness, limited solubility, and rapid degradation necessitate strategic amalgamation with a synthetic polymer. Polyethylene oxide (PEO) is a well-established synthetic polymer in the biomedical field. Its high mechanical properties, solubility, biocompatibility, and biodegradability make PEO a suitable option for polymer blends to address the aforementioned limitations. PEO also exhibits controlled release of loaded materials, which is another reason for its widespread application in biomedical and pharmaceutical fields [35]. Thus, this synergistic blend have designed to ameliorate the overall efficacy of biomedical carriers and mitigate particular challenges inherent to CS [36].

In this novel study, we explored the anti-cancer potential of PEO/CS (PC) NFs incorporating Mn and Li-doped CP-NPs for the first time. Our investigation centered on assessing the efficacy of the engineered scaffold against A375 cells. Additionally, we delved into potential toxic effects on normal fibroblasts, represented by L929 cells.

2. Materials and Methods

2.1. Chemical Substances

Poly(ethylene glycol)-block-poly(propylene glycol) (P123) (EO20-PO70-EO20, MW = 5800 g/mol, Merk, Germany), triethyl phosphate (TEP) (C₆H₁₅O₄P, 99.0%, M.W 182.16, Merck, Germany), Calcium nitrate tetrahydrate (Ca(NO₃)₂*4H₂O, 98.0%, M.W 236.15, Merck, Germany), manganese nitrate tetrahydrate (Mn(NO₃)₂*4H₂O, 98%, M.W. 251.006, Merck,

Germany), lithium nitrate (LiNO₃, 99.99%, M.W. 68.95, Merck, Germany), ammonium hydroxide (NH₄OH (25% w/w)), 75-85% deacetylated chitosan (low M.W 50,000-190,000, Merck, Germany), polyethylene oxide (M.W 100,000, Merck, Germany), and glacial acetic acid (Sigma-Aldrich, USA) were used as precursors for synthesizing NPs and NFs.

2.2. Preparation of CPs

Table 1. To produce 10 grams of particles, an initial step involved dissolving 2 grams of P123 in 100 mL of 99.9% ethanol, which was then stirred at 80°C for one hour. Subsequently, 100 mL of water was added to the polymer substrate. In sequential stages, tetraethyl orthophosphates (TEP), calcium nitrate tetrahydrate, manganese nitrate tetrahydrate, and lithium nitrate were individually introduced into the solution at 60 min intervals. Gel samples were formed by adding 10 cc of ammonium hydroxide and stirring for five hours at 80°C. These gels were left to age at room temperature for 7 days. Subsequent steps involved drying the samples at 70°C for 24 h and then at 140°C for an additional 24 h. The final powders of CP, MnCP, LiCP, and Mn-LiCP were obtained by heating them at 550°C for 24 h, employing a heating and cooling rate of 1°C/min.

Table 1: The designed CPs compositions (mol%).

Sample	Ca	Mn	Li	P
CP	62.5	0	0	37.5
MnCP	46.875	15.625	0	37.5
LiCP	46.875	0	15.625	37.5
Mn-	46.875	7.8125	7.8125	37.5
LiCP				

2.3. NFs Fabrication

For fabricating polymer solutions, a mixture of CS (2.5% w/v) and PEO (15% w/v) was individually stirred and dissolved in 50% v/v acetic acid at room temperature. Following a 24 h

period, the PEO and CS were combined with the volume ratio of 70/30 and further stirred for an additional 24 h. Subsequently, doped NPs were introduced into the solution at determined concentrations (10% and 20% of the polymer weight) and stirred for a duration spanning 24 to 72 h to achieve a homogeneous solution.

The prepared solutions were then transferred to 5ml syringes for electrospinning. The electrospinning machine (Nano Azma, Iran) was employed with specific parameters including a flow rate of 0.4 mL/h, a voltage of 19 KV, a nozzle-to-collector distance of 15cm, and a rotating rate of 400 rpm. To ensure the uniform dispersion of NPs in the polymer matrix, the polymer solutions underwent sonication in a bath (Bandelin, Germany) for 30 min immediately prior to the electrospinning process.

2.4. Characterization of CPs and NFs

2.4.1. X-ray Diffraction (XRD) Analysis

The crystalline phase of CP was examined through X-ray diffraction (XRD) analysis, utilizing the D8-Advance Bruker instrument from Germany. The experimental parameters were configured with a 2θ range spanning $10-80^{\circ}$, employing Cu-K α radiation, a step size of 0.05° , and a time per step of two seconds.

2.4.2. Electron Microscopy for Morphological Observations

The morphological characteristics of both CPs and NFs were examined through Field-emission scanning electron microscopy (FESEM) using a MIRA3 instrument (Tescan, Czech Republic) subsequent to sputter-coating with gold. Additionally, the morphology of the CPs was scrutinized utilizing a transmission electron microscope (TEM) model EM 208S (Philips, Amsterdam, the Netherlands). For the TEM analysis, 0.01 g of the synthesized CPs powder was dispersed in 30 ml

of absolute ethanol through ultrasonic waves (FR USC 22 LQ, 400 w, 20%, Taiwan) for a duration of 10 min. Subsequently, a standard volume of the suspension was collected using a lam. Moreover, PC and NFs with 10% and 20% Mn-LiCP were also examined for their shape and morphology using FESEM.

2.4.3. Ions Release Study

The ion release and concentration fluctuations of Manganese (Mn) and Lithium (Li) from CPs integrated into NFs were assessed through the application of Inductively Coupled Plasma Optical Emission Spectroscopy (ICP-AES) on a Spectro Arcos instrument (Kleve, Germany). To this end, simulated body fluid (SBF) was meticulously prepared following the methodology established by Kokubo [37], and the ensuing protocol of the recent scholarly investigations (37). Subsequent to this preparation, mats were cut into square dimensions of 1×1 cm², immersed in 10 mL of SBF and subjected to controlled agitation employing a Stuart Orbital Shaker (SI500, UK) over time intervals of 1, 3, 7, 14, 21 and 28 days.

2.4.4. Dynamic Light Scattering (DLS) and Zeta Sizer Analysis

Dynamic light scattering (DLS) analysis was conducted using Vasco3 equipment (Cordouan, France) to assess the particle size of the CPs. Surface charge and aggregation characteristics of the synthesized CPs were evaluated through Zetasizer analysis, utilizing the NANO-flex[®] II instrument (Thermo Fisher Scientific, USA). To achieve this, a precise quantity (0.01 g) of CPs was dissolved in absolute ethanol using a probe sonicator (Fisher Scientific, USA) for 10 min to ensure a homogeneous dispersion. Subsequently, the prepared suspension was introduced to the instrument for analysis.

2.4.5. N₂ Adsorption-Desorption Analysis

The specific surface area of the NPs was determined using the Brunauer, Emmett, and Teller (BET) method, following a vacuum degassing process at 250°C for 24 h on the CP powders, conducted by ASSP 2020, USA.

2.4.6. Electro-Fenton's Reaction Analysis

To prepare the working electrode, a mixture of CP powders, polyvinylidene fluoride (PVDF) (Sigma-Aldrich, USA), and carbon black (Sigma-Aldrich, USA) was formulated in a mass ratio of 75:22:3. Initially, 29.4 mg of PVDF was dissolved in 1 mL of 1-methyl-2-pyrrolidinone (NMP) under continuous stirring for 60 min (sol-A). Subsequently, 100 mg of CP particles and 4 mg of carbon black were incrementally introduced into sol-A at 45 min intervals. The resulting solution underwent sonication in a bath for one hour, followed by 24 h of stirring to achieve the desired coating slurry.

For the preparation of the Nickel foam (1 × 0.5 cm²) substrate, the oxidized layer was removed using a 3 M HCl solution, followed by thorough rinsing with alcohol and deionized water. The dip-coated foam in the slurry was then dried through a vacuum process at 80°C for 24 h. Electrochemical properties of the prepared working electrode were assessed using an electrochemical analyzer (Autolab PGSTAT302N). In the testing setup, a platinum (Pt) wire, Ag/AgCl, and a 1 M Na₂SO₄ solution served as the counter electrode, reference electrode, and electrolyte reference, respectively. Notably, electrochemical analysis was conducted in an O₂-saturated electrolyte using a portable oxygen concentrator.

Cyclic voltammetry (CV) analysis of the coated CPs was performed at a scan rate of 50 mV. s⁻¹, and the CV test was conducted in both N₂-purged and O₂-saturated solutions. Electrochemical impedance spectroscopy (EIS) analysis utilized alternating current (AC) with an amplitude of 10

mV in the frequency range of 0.1 Hz–105 Hz. The ZView® software (version 3.5) was employed to derive the solution resistance (Rs), constant phase element (CPE), and charge transfer resistance (Rct) by fitting and simulating the EIS data.

2.4.7. Contact Angel Measurement

The hydrophilicity of NF mats were assessed using contact angle technique (Adeeco, Iran). Aqueous droplets ($2\mu L$) were deposited onto cross-linked PC and PC-20% NFs, and absorption images were subsequently captured.

2.4.8. Water Uptake Assessment

The water uptake properties of NF mats were measured by weighing the samples of 1×1 cm². Subsequently, these pieces were immersed in phosphate-buffered saline (PBS), and subjected to incubation at 37°C for a duration of 24h. Afterwards, the NFs were removed from PBS, placed on filter paper to remove excess water and re-weighed. The swelling degree calculated using the following formula:

Degree of swelling (%) =
$$\left[\frac{(W1-W0)}{(W0)}\right] \times 100$$

Wherein W₁ and W₀ indicates the weights of the swollen and dry NFs after and before soaking in PBS, respectively.

2.4.9. Weight Loss Study

The weight loss of fabricated NFs was measured through dividing them into $(1 \times 1 \text{ cm}^2)$ squares. Subsequently, the segments were weighed, immersed in PBS, and incubated at 37° C up to 28 days. Following removal from PBS, the NF mats underwent a drying process and were re-weighed at

distinct time points, including 1, 3, 7, 14, 21, and 28 days. The weight loss percentage was determined using the following formula:

Weight loss (%) =
$$\left[\frac{(W1-W0)}{(W0)}\right] \times 100$$

Wherein W₁ and W₀ are the weights of the dry NFs after and before soaking in PBS, respectively [38].

2.5. Biological Evaluations of CPs and NFs

2.5.1. Cell Culture

A375 and L929 cell lines, sourced from the National Cell Bank of Iran at the Research Institute of Biotechnology in Mashhad, were cultured in high glucose Dulbecco's Modified Eagle Medium (DMEM) (Gibco, USA). The culture medium was supplemented with 1% penicillin/streptomycin (Pen/Strep) solution (Gibco, USA) and 15% fetal bovine serum (FBS) (Gibco, USA) under standard conditions of 37°C and 5% CO₂ in a humidified atmosphere. The medium was renewed two or three times a week, and the cells were sub-cultured upon reaching 70% confluence. Treatment suspensions were freshly prepared for each experiment. In brief, various concentrations (500, 250, 125 mg/L) of CP solutions were generated by introducing autoclaved CPs into DMEM. This mixture was then incubated in a shaker incubator for 24 h at 37°C. Prior to treatments, the suspensions underwent dispersion using an ultrasonic bath to achieve homogeneity. PC and PC-20% NF mats were UV-sterilized before treatments. For subsequent analyses, the culture medium was entirely removed and the cells were exposed to CP-containing treatment media supplemented with 5% FBS and 1% pen-strep.

2.5.2. Cell Viability Assay

The MTT (3-(4,5-dimethylthiazol-2-yl)-2,5-diphenyltetrazolium bromide) assay was conducted to assess the viability of A375 and L929 cell lines upon their direct exposure to the CPs and NFs. In brief, A375 and L929 cells were seeded in 96-well plates (SPL Life Science, South Korea) at densities of 3×10³ and 4×10³ cells/well, respectively. After 24 h' incubation, the cells were exposed to CP, Mn-CP, Li-CP, and Mn-LiCP at various concentrations, and PC fibers with different percentages of NPs (PC, PC-10% and PC-20%). Subsequently, 0.5 mg/ml MTT was added to the culture media and incubated for 24, 48, and 72 h in darkness. Afterwards, the culture media was gently removed and dimethyl sulfoxide (DMSO) (Merck, Germany) was added and incubated for four hours. The optical density (OD) values were measured using an Epoch microplate reader (BioTek, US) at a wavelength of 570 nm. The cell viability of treated groups was determined by comparing the OD values with the control group.

2.5.3. Flow Cytometry

For the apoptosis assay, the annexin V fluorescein isothiocyanate (FITC)/propidium iodide (PI) apoptosis detection kit (Thermo Fisher Scientific, USA) was employed according to the manufacturer protocol. In brief, A375 and L929 cells were seeded at a density of 1×10⁵ cells/well on separate 6-well plates (SPL Life Science, South Korea). Following 24 h' incubation, the cells were treated by NFs and CPs (with concentrations selected based on MTT results), within media containing 5% FBS and 1% pen-strep. After 72 h, the supernatant was removed and samples were washed twice with PBS before harvesting. The cells were then stained with annexin V-FITC and PI. Finally, the early apoptotic (Annexin V (+)/PI (-)) and late apoptotic (Annexin V (+)/ PI (+)) cells were identified using a flow cytometry (BD, FACS, Calibur USA).

2.5.4. qPCR-Real Time Analysis

2.5.4.1. RNA Extraction and cDNA Synthesis

A375 cells were initially seeded at a density of 3×10⁵ cells/well in 6-well plates. After 24 h, the cells were treated with NFs and a specified concentration of CPs, followed by incubation for 72 h. For the extraction of total RNA, the harvested cells were washed two times with PBS to eliminate potential NP residues. The RNA samples were processed using the RNX Plus solution kit (Sinaclon, Iran) in accordance with the manufacturer's guidelines. The isolated RNA specimens were subsequently assessed both quantitatively and qualitatively using a NanoDrop spectrophotometer (Thermo Fisher Scientific Inc., USA) and through gel electrophoresis on a 1% agarose gel. Upon confirming the quality of the RNA, 1 µg of total RNA was converted into single-strand cDNA using the Easy cDNA Synthesis Kit (Parstous Tech, Iran). The cDNA synthesis process adhered to the manufacturer's guidelines, involving the reversal of extracted RNAs at 47°C for 60 min and subsequent inactivation at 85°C (Applied Biosystems, Thermo Fisher Scientific, USA).

2.5.5. Quantitative PCR (qPCR)

The quantification of TP53, Bax, and Bcl-2 gene expressions was conducted through quantitative polymerase chain reaction (qPCR) using a Real-Time PCR device (Roche, Germany). As shown in **Table 2**, 20 μL reaction mixture consisted of 10 μL of 2X Taq PCR Master Mix (Parstous, Iran), 1 μL of cDNA template, and 5 μM of each primer prepared. The amplification protocol comprised an initial denaturation at 95°C for 15 min, followed by 45 cycles of denaturation at 95°C for 15 s, annealing at 58°C for 30 s, and extension at 72°C for 30 s. Melting curves were generated by gradually increasing the temperature from 65°C to 95°C at a rate of 0.5°C/s. Duplicate runs were executed for all samples. Relative gene expression of the target genes was normalized to GAPDH,

serving as the internal reference. The $2^{-\Delta\Delta Ct}$ method was applied to calculate relative gene expression and fold changes.

Table 2. Primer sequences of real-time PCR test

Gene name	Primer sequences 5' 3'	Product length (bp)
TP53	Forward: GGGAGGACTAAGCGAGCAC	106
	Reverse: TCTCAAGCCCACGGATCTG	. 100
Bax	Forward: CGCCCTTTTCTACTTTGCCAG	07
	Reverse: GAAGTCCAATGTCCAGCCC	9/
Bcl-2	Forward: GGATAACGGAGGCTGGGATG	101
	Reverse: CCAAACCGAGCAGAGTCTTC	101
GAPDH	Forward: GGAAGTCAGGTGGAGCGAG	90
	Reverse: GCCCAATACGACCAAATCAGAG	89

2.5.6. Reactive Oxygen Species (ROS) Assay

A375 cells were assessed for intracellular ROS generation through the utilization of the 2',7'-dichlorofluorescin diacetate (DCFH-DA) staining assay. To this aim, the cells were seeded in 96-well plate at a density of 2.5×10⁴ cells/well and incubated overnight. Afterwards, the medium was removed and the cells were washed with PBS. Subsequently, 25 μL of H₂DCFA, diluted in Dulbecco's Modified Eagle Medium (DMEM), was added to each well, and the cells were incubated for 30 min in the darkness. Following another washing, the cells were treated with CPs and NFs. The fluorescence intensity was then measured at 535 nm and 485 nm after 4 h. For the visualization of ROS production, A375 cells were cultured and treated with either CPs or NFs after reaching 95% confluence for 4 h. Subsequently, the cells were stained with DCFH-DA for 30 min in the dark, washed three times with PBS, and observed under a fluorescence microscope (Optika, IM-3FL4, Italy).

2.5.7. Migration Assay

A Cell Scratch Assay was performed to assess the migratory capacity of A375 and HUVEC (human umbilical vein endothelial cell). The cells were initially seeded at a density of 4×10^4 cells/well in 4-well culture plates until reaching 90–95% confluence. Subsequently, a straight line was carefully scratched onto the cell monolayer using a sterile 10 μ L pipette tip, followed by immediate replacement of the culture media with low-serum (FBS 1%) media. At the next step, the cells were treated with UV-sterilized PC and PC-20% NFs, and incubated for 24 h. The rate of cell mobility was quantified by analyzing the captured images using Image J software.

2.5.8. Blood Compatibility Evaluation

Hemocompatibility assessment of fabricated PC and PC-20% NFs involved placing punched mats into 96-well plates. The human whole blood was ethically obtained under the approval of the Mashhad University of Medical Sciences (IR.MUMS.MEDICAL.REC.1400.453) and collected in citrated tubes. The blood was then diluted in normal saline and deionized water, serving as negative and positive controls, respectively. To assess the hemolysis rate of fabricated scaffolds, 200 µL of whole blood was added to each well and incubated for 120 min at 37°C. Following centrifugation (10 min at 1500 rpm), the supernatant was collected, and absorbance was measured at 545 nm using a microplate reader (Epoch, BioTek, USA). The degree of hemolysis was determined based on the equation:

Hemolysis (%) =
$$\left[\frac{(Ds-Dn)}{(Dp-Dn)}\right] \times 100$$

Wherein Ds, Dn, and Dp represents the absorbance of the samples, negative, and positive controls, respectively [39].

2.6. Statistical Analysis

Quantitative analyses were conducted in triplicate and assessed utilizing GraphPad Prism (version 10.1.2 (324), USA). The results were presented as mean \pm standard deviation (SD). Students t-test, One-way and two-way analysis of variance (ANOVA) were employed, followed by Dunnett and Tukey's tests, respectively. Significance was established for probability values below 0.05 (* P<0.05).

3. Results

3.1. Characterization of Synthesized CPs

3.1.1. FESEM and TEM

The X-ray diffraction (XRD) analysis revealed distinct phases in the examined samples, as depicted in **Figure 1A**. It is evident that the predominant crystalline phase in the CP sample is hydroxyapatite (HAp, Ref. cod. 9-0432). In contrast, the MnCP, LiCP, and Mn-LiCP samples exhibited the presence of β -tricalcium phosphate (β -TCP, Ref. cod. 9-0169), dicalcium phosphate dihydrate (DCPD, "brushite," ref. cod. 9-0077), and dicalcium phosphate anhydrate (DCPA, "monetite," ref. cod. 9-0080) phases. It is noteworthy that a marginal shift of the peaks towards lower angles was observed in all samples when compared to standard references during phase identification.

The results of FESEM are represented in **Figure 1B**, in which alterations in the morphology of CP are evident, displaying the increased crystallinity, particularly in the LiCP sample. The elemental mapping of MnCP in **Figure 1C** sample clarifying the homogenous distribution of dopants. This morphological variation is further corroborated by TEM micrographs in **Figure 1D**. Additionally, a substantial reduction in particle size was observed in the doped samples. As indicated in **Table**

3, the particle size diminishes from 75 nm (CP) to 66 nm (MnCP), 70 nm (LiCP), and 47 nm (Mn-LiCP).

3.1.2. Surface Charge and Specific Surface Area

The corresponding surface charge was increased from -30 mV (CP) to -40 mV (MnCP), -36 mV (LiCP), and -56 mV (Mn-LiCP). The mesoporous characteristics, extracted from nitrogen adsorption-desorption and corresponding Barrett-Joyner-Halenda (BJH) isotherms in **Figure 1E**, are summarized in **Table 3**. The specific surface area (S_{BET}) exhibited a significant increase from 75 m²/g (CP) to 201 m²/g (MnCP), 175 m²/g (LiCP), and 266 m²/g (Mn-LiCP). Furthermore, the pore size diameter underwent a transformation from 45.0 nm (CP) to 2.5 nm (MnCP), 40.4 nm (LiCP), and 20.7 nm (Mn-LiCP), respectively.

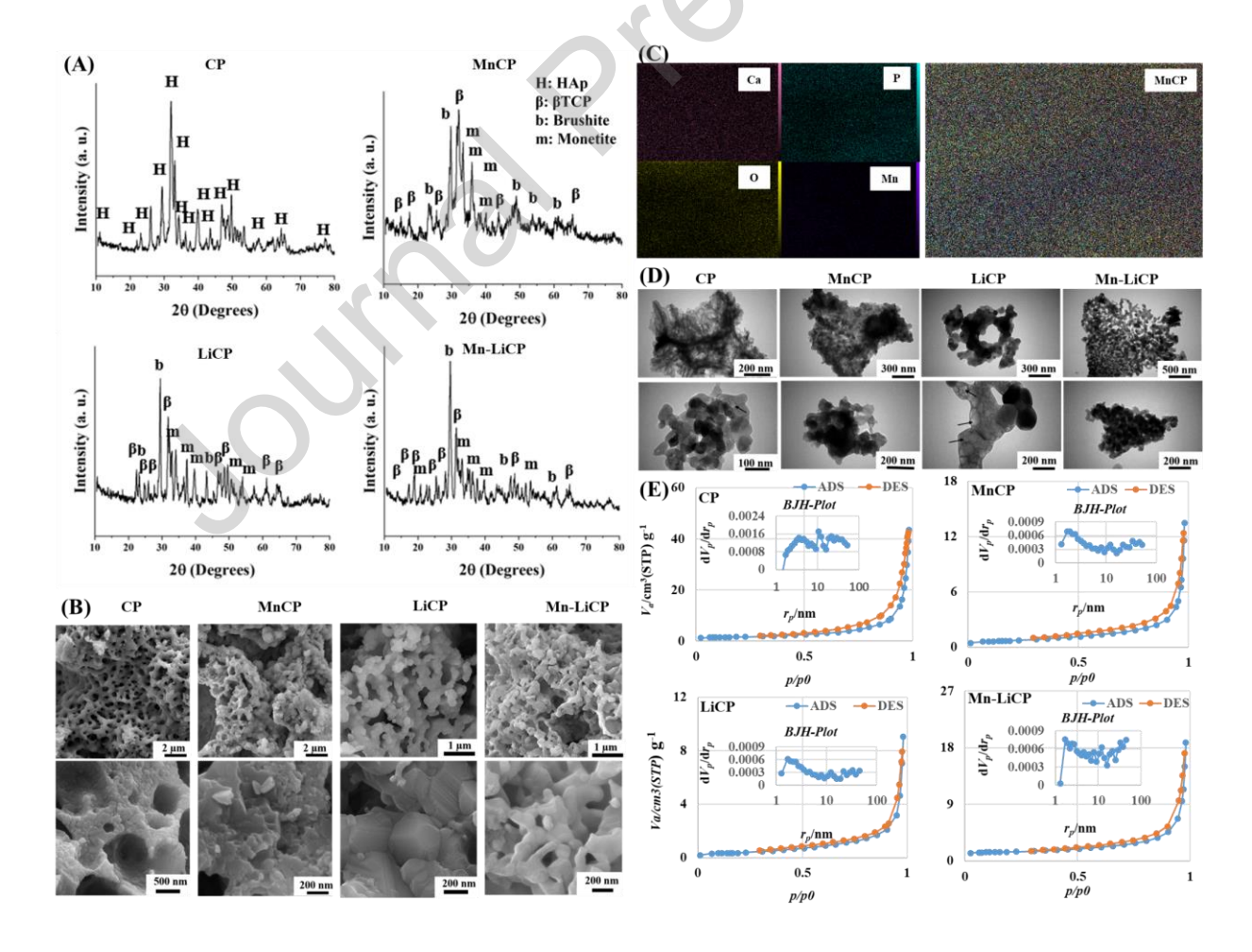


Figure 1. (A) The XRD, (B) FESEM, (C) elemental mapping, (D) TEM, and (E) BET/BJH results of CPs.

Sample	Particle Size (nm)	Zeta potential (mV)	S _{BET} (m ² /g)	Average pore diameter (nm)
CP	75	-30	75	45.0
MnCP	66	-40	201	2.5
LiCP	70	-36	175	40.4
Mn-LiCP	47	-56	266	20.7

3.1.3. **CV-EIS**

To examine the electrochemical characteristics of the specimens, the initial assessment involved evaluating the electrocatalytic activity of freshly fabricated electrodes for both electro-Fenton (EF) and electro-Fenton-like (EF-like) reactions through cyclic voltammetry (CV) in O2 and N2saturated 0.1 M Na₂SO₄ electrolyte. Figure 2A illustrates the CV scans of CP, MnCP, LiCP, and Mn-LiCP electrocatalysts in both O₂-saturated and N₂-saturated electrolytes, with particular focus on the cathodic peak associated with the reduction of O₂, prominently observed in MnCP and Mn-LiCP samples at -0.48 V and -0.6 V, respectively. In Figure 2B, the Nyquist plot of CP, MnCP, LiCP, and Mn-LiCP working electrodes in O2-saturated electrolyte is presented. The electrical equivalent circuits (EEC), encompassing electrolyte resistance (R_s), charge transfer resistance (R_{ct}), and constant phase element (CPE), were fitted to the Electrochemical Impedance Spectroscopy (EIS) data. **Table 4** consolidates the extracted data from the Nyquist plots. Notably, the R_{ct} of Mn-LiCP (4.23×10⁶ Ohm) samples exhibited a marked reduction compared to CP (3.49×10¹² Ohm), MnCP (2.88×10¹¹ Ohm), and LiCP (2.71×10¹¹ Ohm) samples. The calculated K⁰ parameter for the electrodes is tabulated in **Table 4**, where CP, Mn-CP, LiCP, and Mn-LiCP demonstrated values of 0.12×10^{-12} , 0.15×10^{-11} , 0.16×10^{-11} , and 0.10×10^{-6} , respectively.

Table 4. The summarized data of EEC.

Sample	R _s (Ohm)	CPE	R _{ct} (Ohm)	\mathbf{K}^{0}	
СР	65.62	1.73	3.49×10^{12}	0.12×10 ⁻¹²	
MnCP	40.91	0.64	2.88×10^{11}	0.15×10^{-11}	
LiCP	33.38	0.76	2.71×10^{11}	0.16×10 ⁻¹¹	
Mn- LiCP	33.28	0.63	4.23×10 ⁶	0.10×10 ⁻⁶	

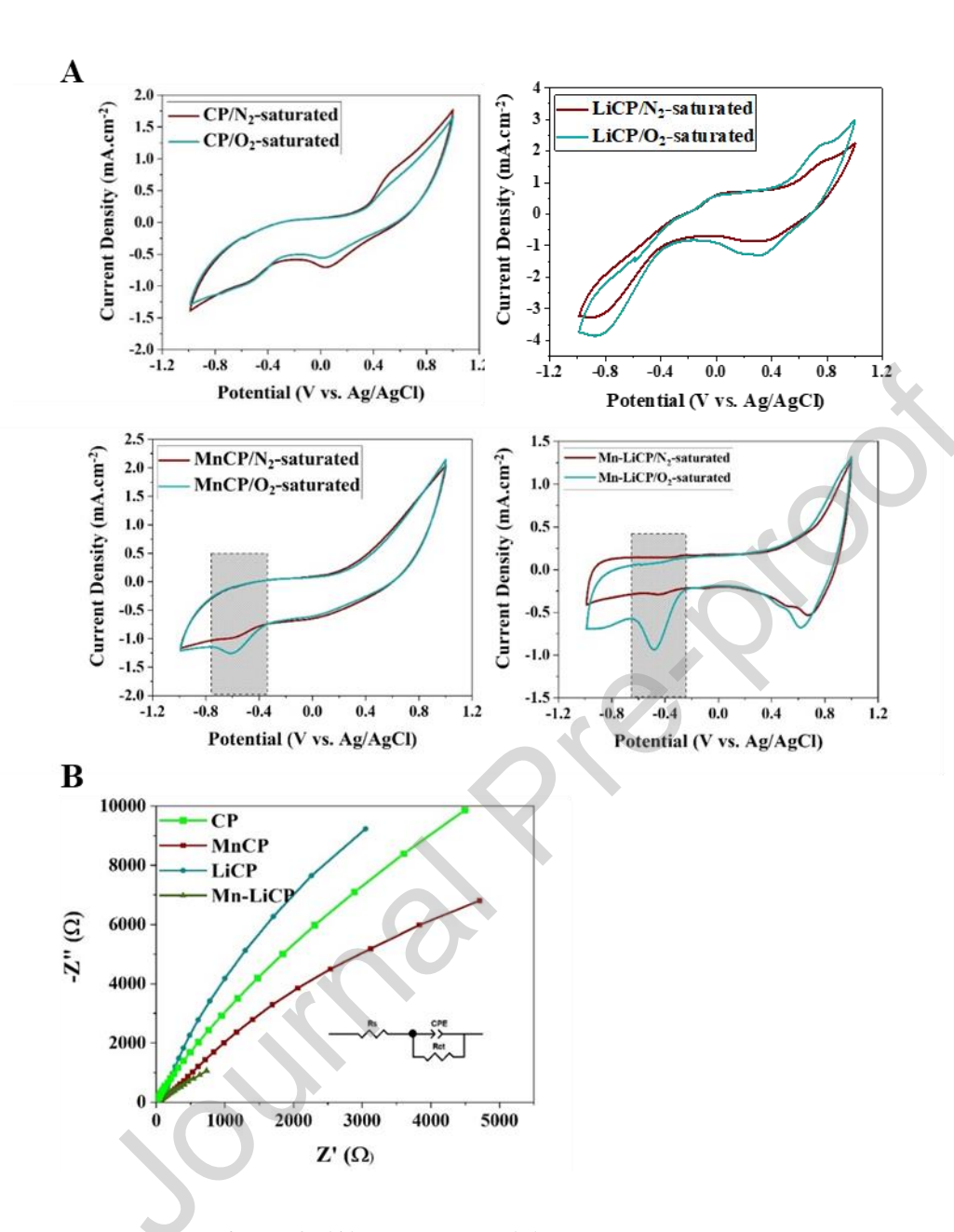


Figure 2. (A) The CV and (B) EIS analysis of the CP electrodes.

3.2. Characterization of NFs

3.2.1. Morphology and Structure of NFs

Based on the FESEM images shown in **Figure 3A**, the NFs of PC, PC-10%, and PC-20% showed a uniform shape with an average diameter of approximately 100 nm. Notably, the electrospun NFs displayed a bead-free morphology with fine interconnected porosity. However, despite sonicating

before and after mixing with the polymer solution, the Mn-LiCP NPs have been agglomerated, which is evident in **Figure 3A**.

3.2.2. Contact Angel, Degradation and Ion Release Profile of NFs

The hydrophilicity characteristics of the electrospun NFs were assessed through a water contact angle (WCA) test, as illustrated in **Figure 3B**. The PC and PC-20% mats exhibited WCAs of 31° and 58° within the first second, gradually diminishing to 22° and 27° over 14 s, respectively. The water absorption (swelling) properties of the fabricated NFs are depicted in **Figure 3C**. The water uptake for PC and PC-20% was measured as 457±26.51% and 495±39.68%, respectively. Additionally, the weight loss of PC and PC-20% fibers after 28 days was recorded as 55.67±4.04% and 51.67±2.08%, as shown in **Figure 3D**. The ion release profile of Mn and Li ions from PC-20% fibers is presented in **Figure 3E**, revealing the highest concentrations of these ions at 1.7 and 2.34 ppm, respectively.

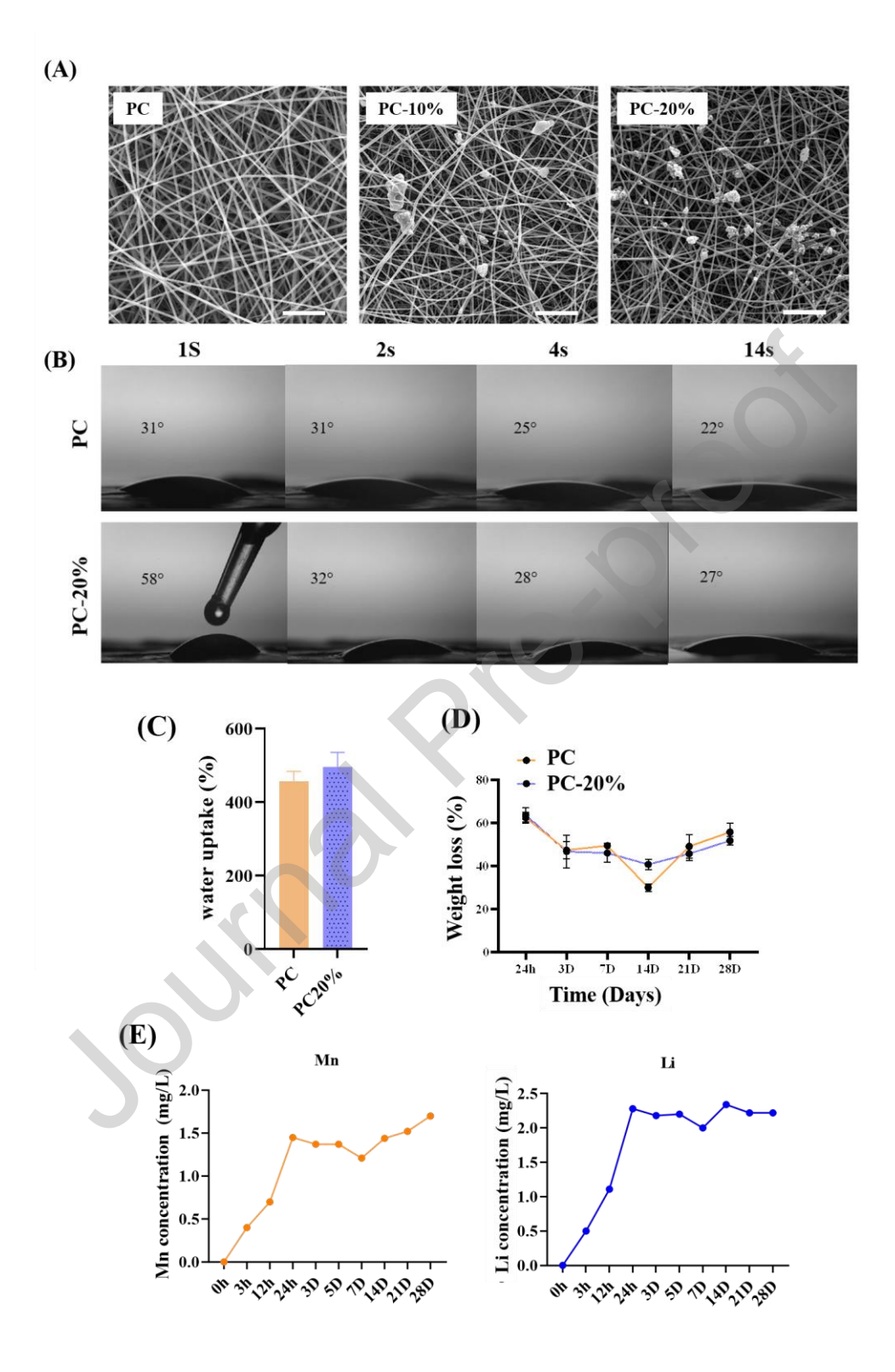


Figure 3. (A) The FESEM, (B) WCA, (C) swelling, (D) degradation, and (E) Mn and Li release of NFs. Data presented as mean \pm standard deviation (n=3). Scale bar 5μ m.

3.3. Biological Properties

3.3.1. MTT Assay

The cytotoxic effects of synthesized CPs were assessed on A375 and L929 cells using the MTT test. As shown in **Figure 4A**, the viability of melanoma cells treated with 125 μ g/mL of CP, MnCPs, and Mn-LiCP particles was significantly decreased to $80 \pm 9\%$, $42 \pm 2.64\%$ and $39 \pm 3.21\%$ (P<0.05) after 72 h post treatment when compared to the control group. Notably, LiCP treatment had no significant toxicity against A375 cells over the same period and concentration ($82 \pm 5.85\%$). Furthermore, the survival rate of L929 cells was significantly enhanced (P<0.05) after 72h when exposed to the synthesized particles, indicated no toxic effects on normal fibroblast cells. However, the viability of L929 cells was significantly reduced when exposed to Mn-LiCP 125 μ g/mL (P<0.05). As shown in **Figure 4B**, it is evident that PC, PC-10%, and PC-20% fibers exhibited no significant cytotoxicity against L929 cells after 72 h. In contrast, these fibers lead to a reduction in viability rates to $82.33 \pm 3.21\%$, $44.33 \pm 3.05\%$, and $32.33 \pm 3.78\%$ in A375 cells after the same duration, respectively.

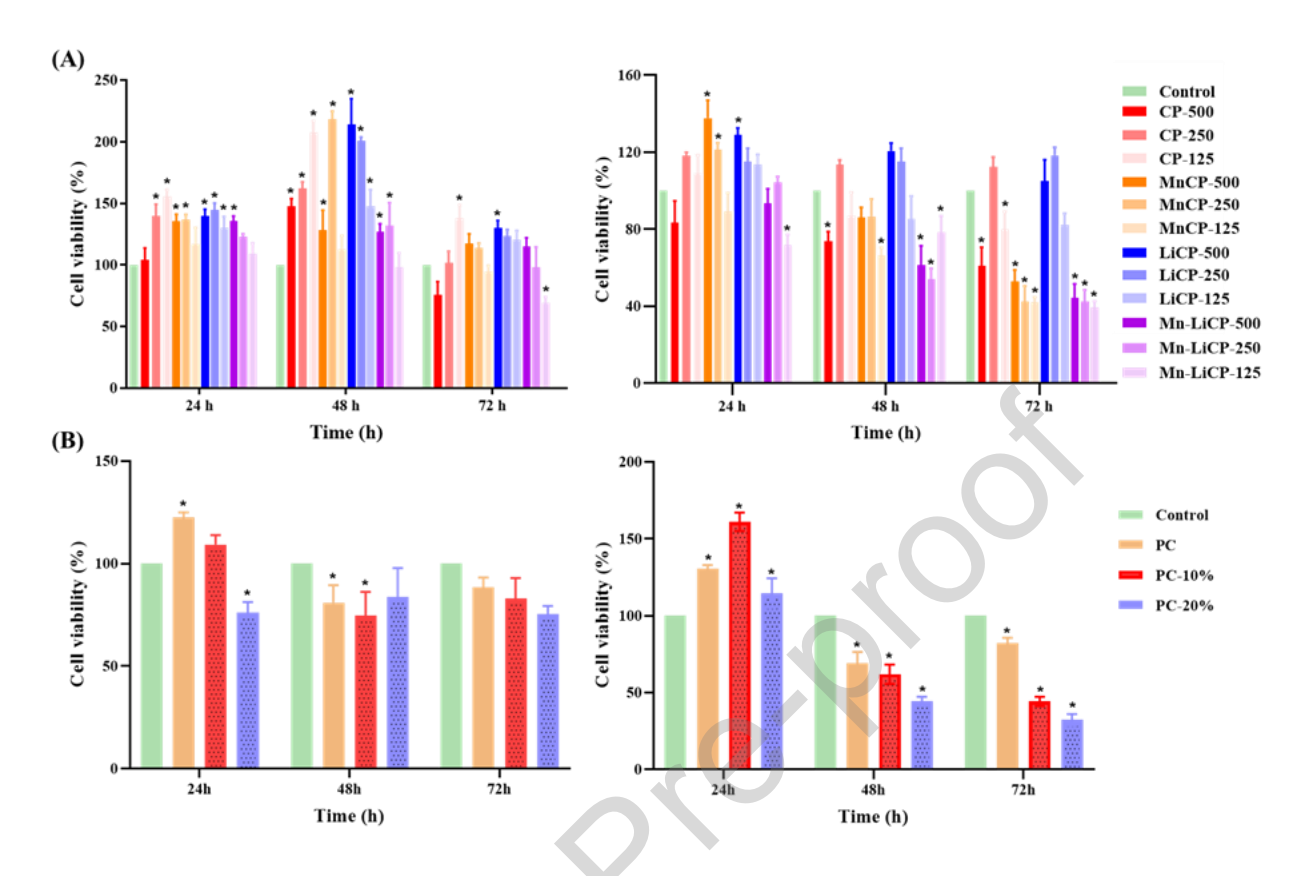


Figure 4. MTT results of **(A)** NPs and **(B)** NFs. Data presented as mean \pm standard deviation (n=3), *P<0.05

3.3.2. Annexin FITC/PI

Figure 5A elucidates that 125 µg/mL treatment had no apoptosis induction effect in L929 cells (**Figure 5B**), while a significant apoptosis was observed in A375 cells when treated with CP, LiCP and Mn-LiCP (19.38 \pm 2.61, 23.2 \pm 2.61 and 40.18 \pm 2.61% respectively, P<0.05) (**Figure 5C**). **Figure 5D** demonstrates the annexin V-FITC/PI results for PC and PC-20%-treated cells. It is notable that the fabricated NFs had no significant apoptotic effect against L929 cells when treated with PC and PC-20% NFs (4.89 \pm 1.87% and 7.76 \pm 1.66%, respectively) (**Figure 5E**). Conversely, in A375 cells, both PC and PC-20% fibers exhibited notable apoptosis rates measuring as 54 \pm 13.15% and 62.55 \pm 4.59%, respectively (**Figure 5F**).

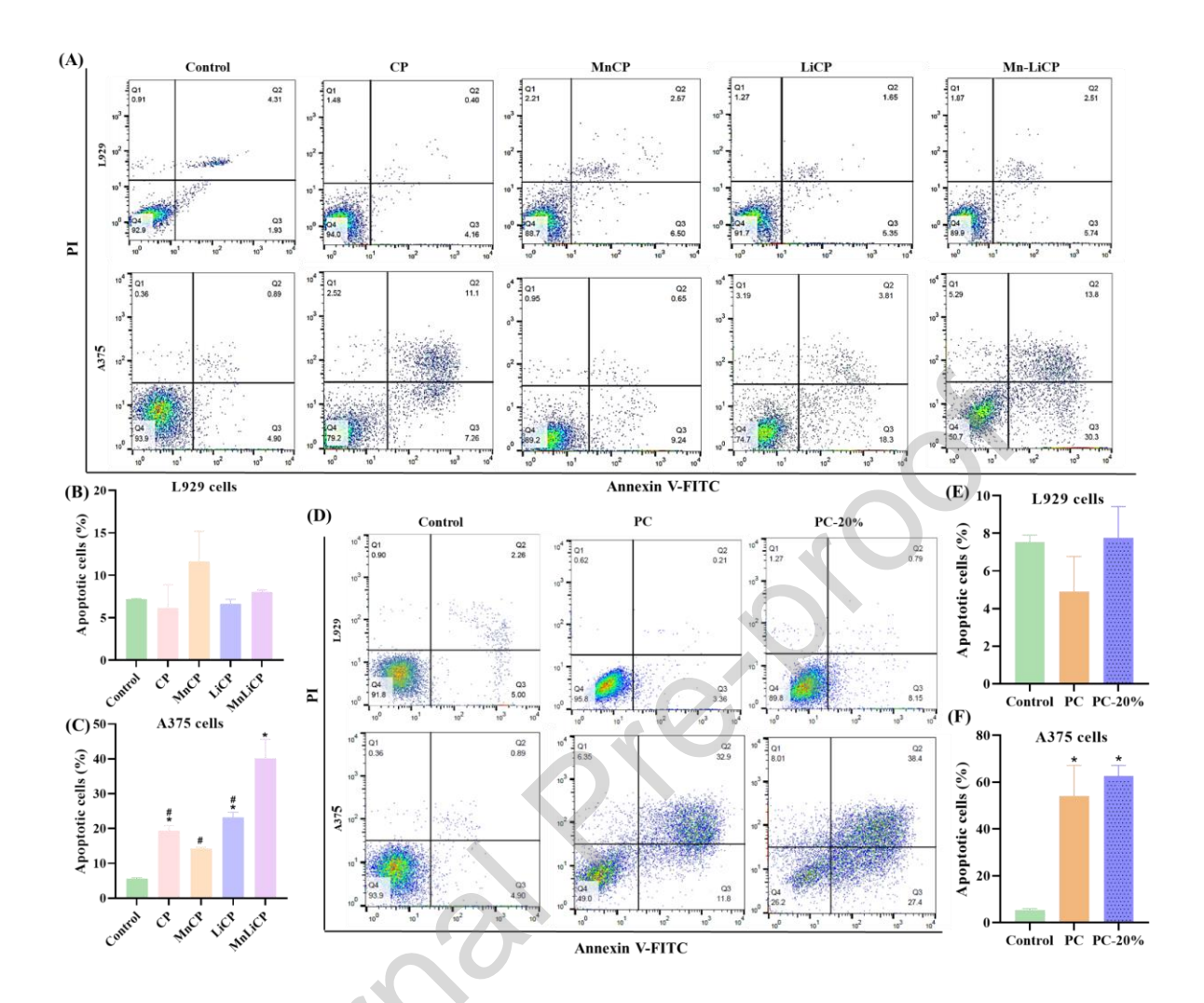


Figure 5. (**A**) The flow cytometry results of annexin V-FITC/PI double stained cells treated with CP, MnCP, LiCP, and MnLiCP as well as control. Quantitative representation of apoptosis rate in NPs-treated (**B**) L929 cells and (**C**) A375 cells after 72 h. (**D**) The flow cytometry results of annexin V-FITC/PI double stained cells treated with PC and PC-20% NFs. Quantitative data regarding the apoptosis percentage of NFs-treated (**E**) L929 cells and (**F**) A375 cells. Data presented as mean ± standard deviation (n=3), *P<0.05 compared to control group and #P<0.05 compared to Mn-LiCP group.

3.3.3. qPCR

The obtained results from quantitative polymerase chain reaction (qPCR) demonstrated the relative mRNA expressions of pro-apoptotic (P53, Bax) and anti-apoptotic (Bcl-2) genes in A375 cells exposed to diverse types of CP-NPs, as depicted in **Figure 6A**. The findings revealed a significant upregulation in P53 (6.06 ± 0.9 , 4.6 ± 0.7 and 6.23 ± 0.3) and Bax (5.3 ± 0.5 , 7.92 ± 0.1 , and 6.38 ± 0.4) gene expression in A375 cells treated with MnCP, LiCP and Mn-LiCP, respectively

(P<0.05). Additionally, the relative Bcl-2 gene expression was substantially enhanced (3.95 \pm 0.2, 2.45 \pm 0.4, 3.84 \pm 0.3) in the cells treated with CP, MnCP and LiCP (P<0.05), respectively. In addition, the ratio of Bax/Bcl-2 expression (which represents a cell death switch) was calculated to determine the life or death of cells in response to the apoptotic stimulus (NPs) [40]. Among treated NPs, Mn-LiCP revealed a significant increase in Bax/Bcl-2 ratio (3.63 \pm 0.3) when compared with other groups. **Figure 6B** portrays the analysis of pro-apoptotic (p53, Bax) and antiapoptotic (Bcl-2) gene expressions of cells treated with final fabricated mats, which reveals a significant augmentation in the expression of pro-apoptotic genes (P53, Bax) along with Bcl-2 within A375 cells; however, the ratio of Bax/Bcl-2 was only significantly increased in cells treated with P-20% mats (P<0.05).

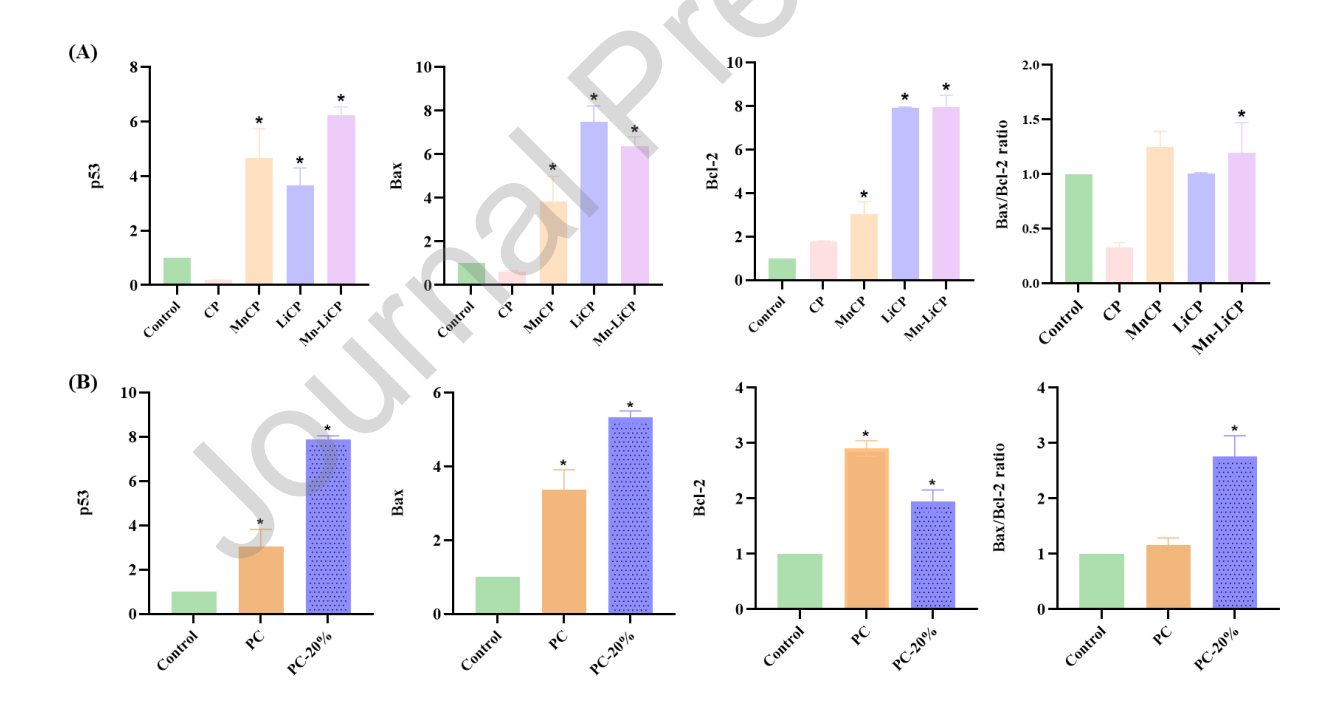


Figure 6. Apoptotic gene expression profile of A375 cells after 72h treatment with **(A)** CP-NPs and **(B)** NFs. Data presented as mean ± standard deviation (n=3), *P<0.05

3.3.4. ROS staining

Figure 7 illustrates the ROS generation in A375 cells induced by NPs and NFs. Excessive ROS production was monitored utilizing the DCFH-DA reagent. This dye exhibits heightened fluorescence in the presence of intracellular oxidative stress. As shown in **Figure 7**, cells treated with Mn-CP, Li-CP, MnLi-CP, and PC-20% demonstrated an intensity of 601 ± 22 , 353 ± 22 , 707 ± 22 , and 727 ± 28 units, respectively.

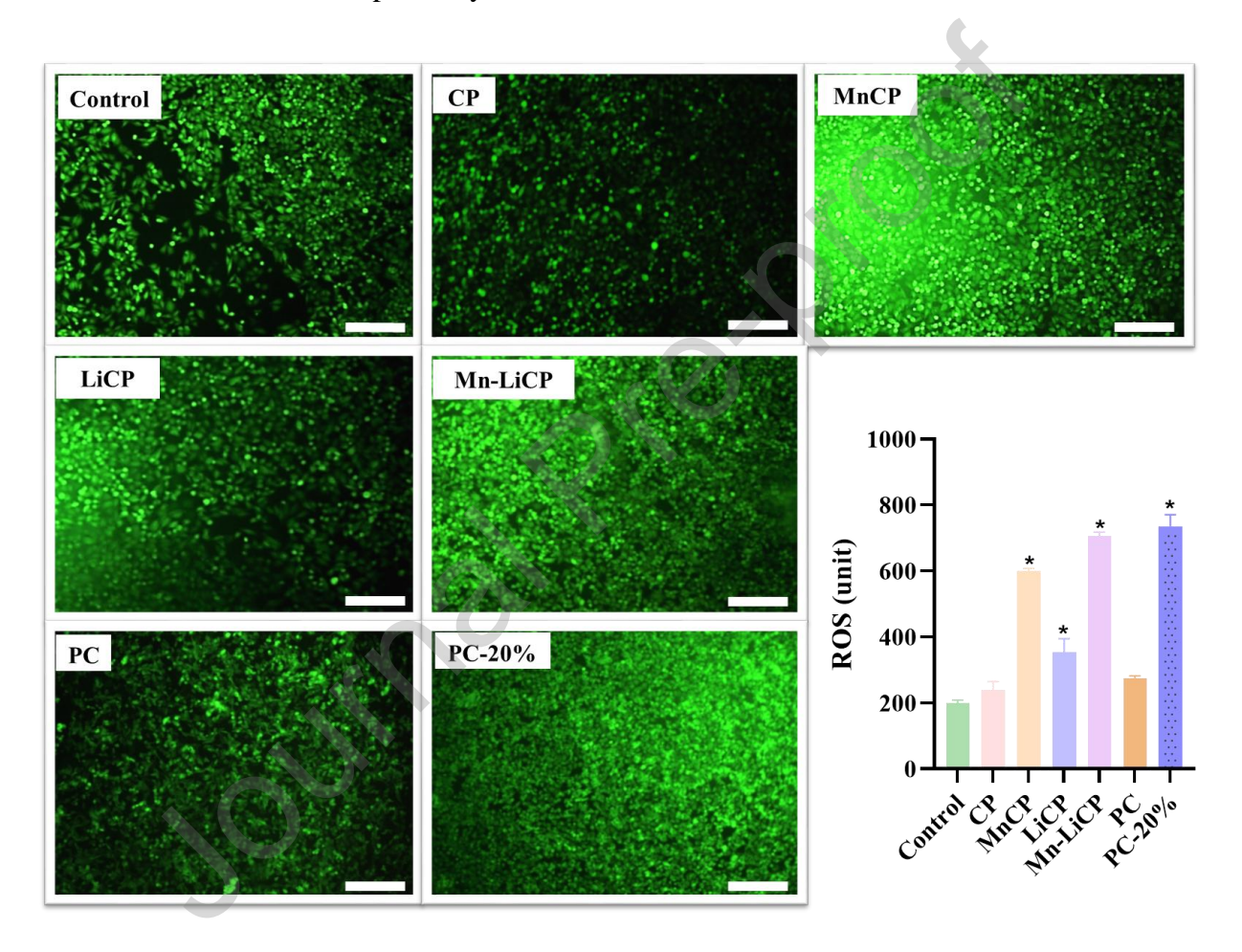


Figure 7. Measurements of ROS production and fluorescent images of A375 cells treated with different samples. Data presented as mean \pm standard deviation (n=3), *P<0.05, Scale bar: 100 μ m.

3.3.5. Cell Migration and Blood Compatibility Assays

The cell scratch assay was conducted to assess the migratory behavior of A375 and HUVEC cells exposed to PC and PC-20% fibers, as illustrated in **Figure 8A**. The results revealed that PC mats

had significant reduction in motility and migration of A375 cells (-3 \pm 1) upon exposure to fabricated mats when compared with control group. Notably, PC-20% mats exhibited widespread apoptosis among A375 cells 24h (**Figure 8B**). In contrast, HUVEC cells showed a slight decrease in migration rate, when exposed to PC-20% mats; however, this increase wasn't statistically significant (**Figure 8C**).

Figure 8D represents the blood compatibility of PC and PC-20% NFs. The hemolysis rates for these samples were found to be $2.97 \pm 0.7\%$ and $0.4 \pm 0.7\%$, in comparison to the positive control, respectively.

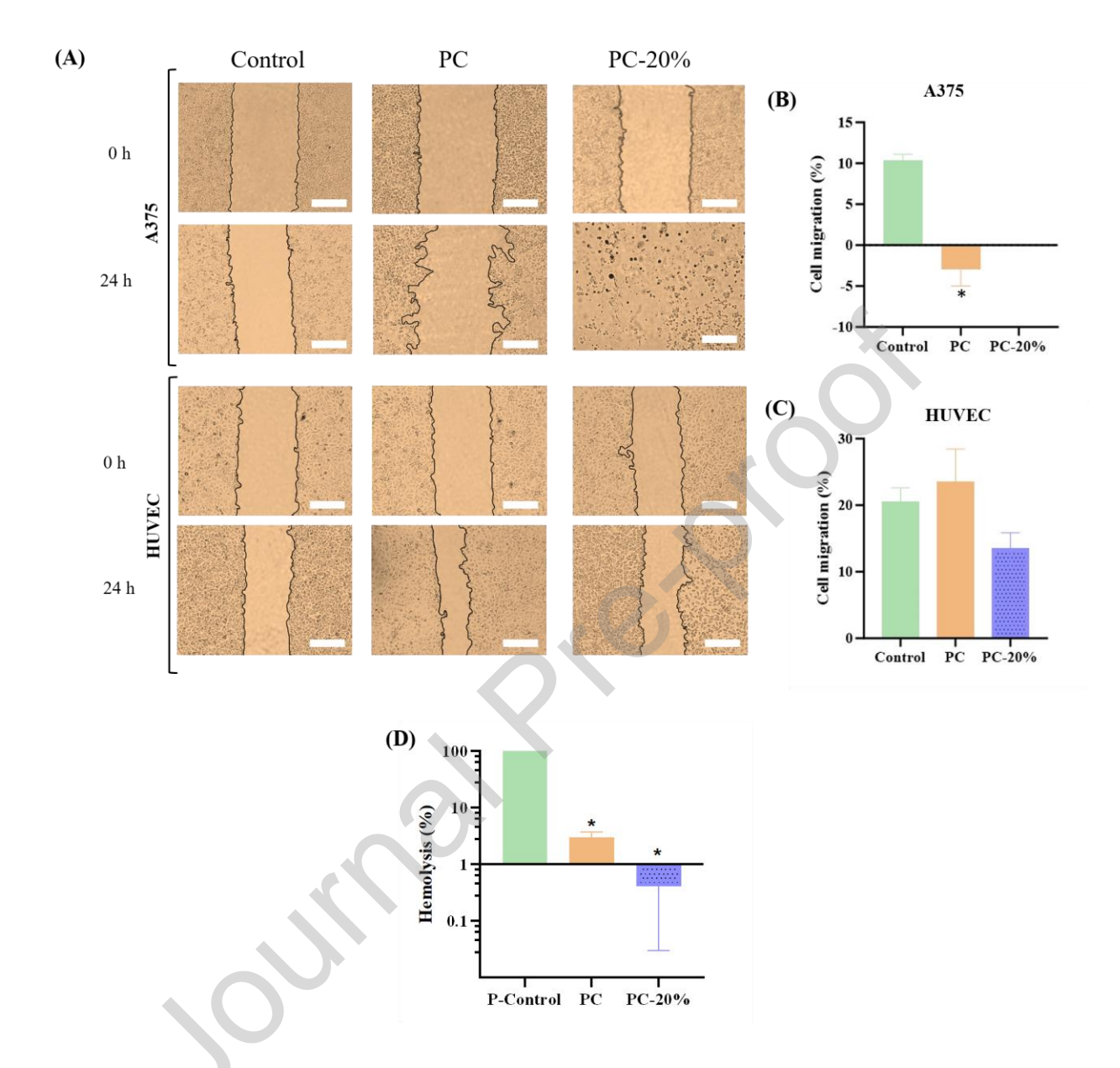


Figure 8. Represents (**A**) Cell scratch assay images of A375 and HUVEC cells, Quantitative data regarding the migration percentage of (**B**) A375 cells and (**C**) HUVEC cells. (**D**) Hemocompatibility results of PC and PC-20% fibers in contrast to the control group. (P-control: positive control). Data presented as mean \pm standard deviation (n=3), *P<0.05 Scale bar: 100 μ m.

4. Discussion

Numerous studies have confirmed the therapeutic potential of calcium phosphates either directly by itself or as a carrier for other therapeutic agents for cancer treatment. For instance, Dong et al.

demonstrated that doxorubicin-loaded nano-hydroxyapatites (nHAp) exhibited a synergistic effect against multidrug-resistant breast cancer MCF-7/ADR cells, surpassing the efficacy of free doxorubicin. This formulation effectively inhibited tumor growth in animal models, mitigating side effects associated with standalone doxorubicin administration [41]. In a similar vein, Govindan et al. synthesized magnetic calcium phosphates, incorporating andrographolide, an anticancer drug. The results indicated heightened anti-proliferative and anti-apoptotic activities against A431 cell lines when andrographolide was combined with magnetic calcium phosphates [42].

In the present study, we synthesized a series of CPs containing manganese and lithium, as detailed in **Table 1**. The design yielded four distinct groups of CPs, including I) CP: Ca₅(PO₄)₃OH, II) Mn_{2.5}Ca_{2.5}(PO₄)₃OH, III) LiCP: Li_{2.5} Ca_{2.5}(PO₄)₃OH, and IV) Mn-LiCP: Li_{1.25}Mn_{1.25}Ca_{2.5}(PO₄)₃OH. As anticipated, the crystallized phase in group I corresponded to hydroxyapatite (Figure 1A). Conversely, the Ca/P ratio decreased from 1.67 to 0.834 in the remaining groups. Notably, the (Ca + M)/P ratio was maintained at 1.67 across all groups, leading to the expected formation of CPs with reduced Ca/P ratio or phases containing substitute elements. Our phase identification results (**Figure 1A**) revealed the presence of brushite, monetite, and βtricalcium phosphate with Ca/P ratios of 1, 1, and 1.5, respectively, in the other groups. Peaks related to manganese and lithium phases were not observed, suggesting their potential presence as precursors in the amorphous regions, such as amorphous calcium phosphates (ACP), a phenomenon observed elsewhere [8]. The morphology analysis (**Figure 1 B-D**), N₂-adsorptiondesorption isotherms (Figure 1E), and physicochemical properties (Table 3) exhibited distinctive enhancements in the Ca-substituted structures, particularly in those with both manganese and lithium substitutions.

The enhanced properties can be attributed to the disturbance caused by the substitution of elements

in CaPs, leading to increased repulsion forces between particles and a subsequent decrease in agglomeration [43, 44]. Notably, the high surface charge of the substituted particles, exemplified by -56 mV for Mn-LiCP, is indicative of substantial improvement in biological performance, particularly during the initial stages of cellular reactions. The mesoporous nature of all CPs displayed a significant increase in specific surface area (from 75 to 266 m²/g), attributed to improvements in particle morphologies.

Furthermore, BJH analysis indicated a mesoporous nature with varying pore diameters (ranging from 2 nm to 50 nm) and multi-peak BJH graphs, suggestive of a disordered mesoporous structure, as proposed elsewhere [16, 45]. This disordering is attributed to the role of substitution elements in disrupting the structure, potentially altering the electrochemical and biological aspects of the particles.

This study primarily focused on investigating the electrochemical properties of substituted CPs. In EF and EF-like reactions, O₂ undergoes conversion to either OH⁻ or H₂O, contingent upon the electrolyte pH (see reactions A-F). The cathode surface in EF and EF-like reactions follows two pathways: (I) a partial two-electron reduction leading to H₂O₂ formation (see reactions **E** and **F**), and (II) a direct four-electron reduction resulting in H₂O formation (see reaction **D**). Manganese oxides, particularly MnO₂, and iron oxides, especially Fe₂O₃, have been identified as promising electrode materials for EF and EF-like reactions compared to transition metal oxides.

The cyclic voltammetry (CV) curves of MnCP and Mn-LiCP samples revealed a cathodic peak corresponding to O₂ reduction (Figure **2A** and reaction **E**) in O₂-saturated electrolytes, while no such peak was observed in N₂-saturated conditions. According to existing literature, an increase in the cathodic peak potential indicates heightened activity in EF and EF-like processes. Consequently, the Mn-LiCP sample, with a more positive cathodic peak potential (-0.48 V),

demonstrated increased activity in EF and EF-like processes as compared to MnCP (-0.60 V). This implies that the Mn-Li-MnO₂ electrode serves as an effective EF-like electrocatalyst for generating O₂ free radicals and H₂O₂. The superior performance of Mn-LiCP over MnCP is attributed to the enhanced physicochemical properties and superior ion-electron transfer in the complex structures of the former.

Reactions in alkaline aqueous solution:

i. Four electron pathways

$$O_2 + H_2O + 4e^- \rightarrow 4OH^-$$

Reaction A

ii. Two electron pathways

$$O_2 + H_2O + 2e^- \rightarrow HO_2^- + OH^-$$

Reaction B

$$HO_2^- + H_2O + 2e^- \rightarrow 3OH^-$$

Reaction C

Reactions in acidic aqueous solution:

i. Four electron pathways

$$O_2 + 4H^+ + 4e^- \rightarrow H_2O$$

Reaction **D**

ii. Two electron pathways

$$O_2 + 2H^{\scriptscriptstyle +} + 2e^{\scriptscriptstyle -} \longrightarrow H_2O_2$$

Reaction **E**

$$H_2O_2 + 2H^+ + 2e^- \rightarrow 2H_2O$$

Reaction F

The electrocatalytic activity (EF) is significantly influenced by the electron transfer rate from the catalyst to the substrate. To delve into the interference properties and kinetics of EF, as well as EF-like reactions, electrochemical impedance spectroscopy (EIS) was employed. For a

comprehensive understanding of the electrode/electrolyte interface, appropriate electrical equivalent circuits (EEC) were fitted to the EIS data, encompassing electrolyte resistance (Rs), charge transfer resistance (Rct), and constant phase element (CPE) (**Figure 2B**).

In EF and EF-like systems, the diffusion of not only O2 but also metal cations into the electrode surface is imperative, as established by previous studies. Analyzing the charge transfer on the electrode surface/electrolyte and the diffusion within the electrode surface was facilitated by calculating the R_{ct} parameter from EIS data. The R_{ct} values were crucial for comparing the kinetics of different electrodes, as summarized in Table 4, which presents fitted data, including Rs, Rct, and CPE from Nyquist plots for various working electrodes. Notably, in the case of CP samples, the charge transfer resistance of the Mn-LiCP sample showed a significant reduction compared to other samples. This reduction in Rct for Mn-LiCP can be attributed to factors such as the small particle size (47 nm) and the well-dispersion of Mn-LiCP, leading to a minimized interfacial resistance of charge transfer. Furthermore, the standard rate constant (K⁰) of the EF reaction, inversely proportional to the calculated Rct from EIS data, was assessed and presented in **Table 4**. The Mn-LiCP sample exhibited the highest K⁰ value (0.10×10⁻⁶), indicating superior EF and EFlike activity compared to other samples. This enhancement in activity can be attributed to the cathodic peak of reduction O₂ in O₂-saturated solution, along with improvements in R_{ct} and K⁰ derived from EIS data, as elucidated in our prior study [23].

We have incorporated Mn-LiCP particles into CS and PEO, forming CP fibers. The FESEM results in **Figure 3A** demonstrated a homogeneous and well-dispersed arrangement of particles within the fibers. These fibers exhibited favorable wettability (**Figure 3B**), crucial for early cell attraction. The swelling data (**Figure 3C**) for PC and PC 20% reveal high water adsorption up to 457% and 495%, respectively, vital for diverse drug delivery applications. It should be highlighted that a

balanced rate between scaffold degradation and tissue regeneration should be preserved. In this regard, our weight loss results showed a degradation rate exceeding 50% after 28 days for both PC PC and 20%, indicating positive tissue development. Examining Mn and Li release from the fibers, acting as therapeutic ions, we observed a burst release in the first 24 h followed by a steady prolonged release up to 28 days (Figure 3D). The released ions suggest the suitability of these fibers for sustained therapeutic release. The release of Mn also plays a pivotal role in an EF-like reaction, signaling the activation of the apoptosis pathway through irreversible opening of mitochondrial permeability transition pores (11). To assess the toxic effects of NPs on L929 and A375, we conducted an MTT assay. Figure 4A indicates that NPs have no adverse effects on normal L929 cell proliferation, instead promoting viability after 72 h, underscoring the high cytocompatibility of the synthesized particles. Conversely, a significant decrease in A375 cell viability was observed after 72 h, with MnCP and Mn-LiCP NPs showing a 52% and 44% decrease, respectively. These findings align with previous studies demonstrating the efficacy of Mn-doped HAp against breast cancer cells and bufalinloaded hollow MnO₂ particles in targeted treatment against H22 cells (liver cancer) [19, 46]. The lower H₂O₂ levels in normal microenvironments compared to TME may explain the toxicity of Mn-containing NPs in the latter, attributed to the generation of free radicals via EF. Furthermore, cell viability was significantly decreased when particles were incorporated into the mats (Figure **4B**). In this sense, the higher toxicity against A375 cells attributed to the synergistic anticancer effect of CS and the particles; PC-10% and PC-20% fibers exhibited 44% and 32% cell viability, respectively. The same results were observed when 4T1, A-431 and CACO-2 cells were exposed to free nHAps, and when combined with Doxurubicin (in contrast to control group and when used doxorubicin alone) by Ramirez et al. and salahuddin et. al. [47, 48].

To elucidate the cell death mechanism in A375 cells, Annexin/PI staining and flow cytometry were conducted for both cell lines (see **Figure 5**). The results revealed a noteworthy increase apoptosis within Mn-LiCP-treated groups ($40 \pm 5.42\%$), as well as in LiCP and CP groups (23% and 19%, respectively). The synergistic toxic impact of Mn-LiCP particles, when combined with chitosan, was evident in PC-20% NFs, resulting in a notable increase in apoptosis up to 65%. These outcomes align with previous studies by Wang et al., Park et al., and Abedian et al., which reported apoptosis as the cell death mechanism induced by Mn-containing NPs and chitosan in various cancer cell lines (MDA-MB-231, H22, Saos-2, HeLa) [19, 46, 49]. To corroborate these findings, quantitative PCR (qPCR) was employed as a complementary test (refer to Figure 6A). Further investigation into pro and anti-apoptotic gene expression (P53, Bax, and Bcl-2) unveiled mitochondrial-dependent apoptosis in A375 cells. A substantial rise in P53 and Bax mRNA levels was observed in MnCP, LiCP, and Mn-LiCP-treated cells. Although an increase in Bcl-2 expression was noted in the aforementioned NPs, the elevated Bax/Bcl-2 ratio rendered A375 cells susceptible to triggering the apoptosis process (see Figure 6B) [50]. PC-20% NFs exhibited a parallel significant increase in P53, Bax and Bcl-2 gene expression, in which Bax/Bcl-2 ratio was significant in PC-20% treated cells, reinforcing the earlier findings [51]. These results align with Xu et al.'s work, wherein chitosan-based hydrogels containing hydroxyapatite activated the intrinsic apoptosis pathway both in vitro and in vivo [52].

Measurement of reactive oxygen species (ROS) production through DCFH oxidation and fluorescent imaging in particles and fibers confirmed the impairment of the antioxidant defense system, elevated ROS levels, and facilitation of mitochondrial impairment (see **Figure 7**). The observed results were statistically significant in cells treated with Mn-containing particles and fibers.

The migration and metastasis of tumor cells play a pivotal role in tumor recurrence and treatment failure. The impact of the finalized PC-20% NFs on A375 cell migration was assessed using a cell scratch assay (see **Figure 8A**). A substantial decrease in A375 cell migration and apoptosis was observed upon exposure to PC, particularly PC-20% NFs, attributed to the combined toxicity of CS and Mn. These findings align with previous studies by Wang et al., Li et al., and Zhang et al., where hydroxyapatites, lithium chloride, and manganese oxide-coated NPs significantly inhibited cancer cell migration (A549, OS-732) [27, 53, 54]. Endothelial cells play determining role during angiogenesis process. Therefore, HUVECs can be the best model to evaluate scaffolds potential for in vitro progression of neovascularization and angiogenesis. Fabricated fibers didn't show significant increase/decrease of HUVEC cells' migration; compared with control group. However, a slight decrease in migration of HUVECs was seen in PC-20% fiber-treated group. This decrease can be attributed to the role of Li in blocking TGFBIp (transforming growth factor-β-induced protein) expression and TGFBIp-induced lymphangiogenesis [55]. This finding encourages that fabricated mats can cease angiogenesis; which is a crucial step during metastasis of primary tumor cells. To evaluate the biosafety of the manufactured PC and PC-20% NFs, the hemolysis potential of mats was examined (see Figure 8B). The results affirmed the high compatibility of Mn-LiCPcontaining NFs with red blood cells, with a hemolysis percentage of 0.4%, conforming to ASTM F 756-00 (2000) standards.

5. Conclusions

In summary, our study has focused on enhancing the efficacy of cancer therapy through the incorporation of therapeutic elements, specifically manganese (Mn), into calcium phosphates. Utilizing the advanced technique electrospinning we could successfully develop materials with remarkable cytotoxic effects on cancer cells. The induced apoptosis, observed through various

assays such as Annexin V/PI and qPCR analysis of pro-apoptotic and anti-apoptotic genes, underscores the potential of our approach in promoting targeted cancer treatment. The physicochemical characterization of these materials revealed favorable properties, including a well-defined particle size (47-75 nm), appropriate surface charge ((-56)-(-30) mV), and specific surface area (75-266 m²/g). The electrochemical analysis demonstrated the capability of Mn and Mn-Li-doped calcium phosphates to serve as effective electrocatalysts, generating O₂ free radicals and H₂O₂, crucial for cancer cell inhibition. In conclusion, our comprehensive investigation highlights the promising role of electrospun calcium phosphates with manganese and lithium doping as a formidable strategy in cancer therapy. The multifaceted positive attributes of these materials position them as potential candidates for further development and application in targeted cancer treatment modalities.

CRediT authorship contribution statement: Sara Gorgani: Methodology, Software, Writing - original draft. Farzad Kermani: Writing - original draft, Methodology, Formal analysis. Khatereh Sadeghzadeh: Methodology. Arghavan Vojdani: Data curation, Methodology. Sara Hooshmand: Investigation, Writing — review and editing. Kobra Fouroughi: Software, Validation. Zoleikha Azari: Investigation. Seyede Atefe Hosseini: Investigation, Sahar Mollazadeh: Project administration, Validation. Alireza Ebrahimzadeh Bideskan: Supervision, Resources, Writing — review and editing. Simin Nazarnezhad: Supervision, Funding acquisition, Validation, Writing — review and editing.

Declaration of competing interest: The authors declare that they have no known competing financial interests or personal relationships that could have appeared to influence the work reported in this paper.

Acknowledgement: This research was supported by the Mashhad University of Medical Sciences through Grant Number 4001539.

References

- [1] R. L. Siegel, K. D. Miller, N. S. Wagle, and A. Jemal, "Cancer statistics, 2023," *Ca Cancer J Clin,* vol. 73, no. 1, pp. 17-48, 2023.
- [2] F. B. Ahmad and R. N. Anderson, "The leading causes of death in the US for 2020," *Jama*, vol. 325, no. 18, pp. 1829-1830, 2021.
- [3] H. Sung *et al.*, "Global cancer statistics 2020: GLOBOCAN estimates of incidence and mortality worldwide for 36 cancers in 185 countries," *CA: a cancer journal for clinicians*, vol. 71, no. 3, pp. 209-249, 2021.
- [4] K. Saginala, A. Barsouk, J. S. Aluru, P. Rawla, and A. Barsouk, "Epidemiology of melanoma," *Medical sciences*, vol. 9, no. 4, p. 63, 2021.
- [5] A. Mohammadpour, M. Derakhshan, H. Darabi, P. Hedayat, and M. Momeni, "Melanoma: where we are and where we go," *Journal of cellular physiology*, vol. 234, no. 4, pp. 3307-3320, 2019.
- [6] F. Sabir, M. Barani, A. Rahdar, M. Bilal, and M. Nadeem, "How to face skin cancer with nanomaterials: A review," *Biointerface Res. Appl. Chem,* vol. 11, no. 4, pp. 11931-11955, 2021.
- [7] M. Bilal and H. M. Iqbal, "New insights on unique features and role of nanostructured materials in cosmetics," *Cosmetics*, vol. 7, no. 2, p. 24, 2020.
- [8] F. Kermani, S. Kargozar, Z. Tayarani-Najaran, A. Yousefi, S. M. Beidokhti, and M. H. Moayed, "Synthesis of nano HA/βTCP mesoporous particles using a simple modification in granulation method," *Materials Science and Engineering: C*, vol. 96, pp. 859-871, 2019.
- [9] S. Genç and N. Türkoğlu, "Labeling MCF-7 cell line with interleukin-6/calcium phosphate nanoparticles," *Nano Biomedicine and Engineering*, vol. 15 (1),p. 51, 2023.
- [10] L. H. Fu, C. Qi, T. Sun, K. Huang, J. Lin, and P. Huang, "Glucose oxidase-instructed biomineralization of calcium-based biomaterials for biomedical applications," in *Exploration*, 2023, vol. 3, no. 6, p. 20210110: Wiley Online Library.
- [11] S. Kargozar *et al.*, "Hydroxyapatite nanoparticles for improved cancer theranostics," *Journal of Functional Biomaterials*, vol. 13, no. 3, p. 100, 2022.
- [12] F. Kermani, S. Kargozar, S. V. Dorozhkin, and S. Mollazadeh, "Calcium phosphate bioceramics for improved angiogenesis," in *Biomaterials for Vasculogenesis and Angiogenesis*: Elsevier, 2022, pp. 185-203.
- [13] M. Šupová, "Substituted hydroxyapatites for biomedical applications: A review," *Ceramics international*, vol. 41, no. 8, pp. 9203-9231, 2015.
- [14] C. Qi, J. Lin, L.-H. Fu, and P. Huang, "Calcium-based biomaterials for diagnosis, treatment, and theranostics," *Chemical Society Reviews*, vol. 47, no. 2, pp. 357-403, 2018.
- [15] F. Kermani, S. Mollazadeh, S. Kargozar, and J. V. Khakhi, "Improved osteogenesis and angiogenesis of theranostic ions doped calcium phosphates (CaPs) by a simple surface treatment process: A state-of-the-art study," *Materials Science and Engineering: C,* vol. 124, p. 112082, 2021.
- [16] F. Kermani, S. Mollazadeh, S. Kargozar, and J. V. Khakhi, "Solution combustion synthesis (SCS) of theranostic ions doped biphasic calcium phosphates; kinetic of ions release in simulated body fluid (SBF) and reactive oxygen species (ROS) generation," *Materials Science and Engineering: C*, vol. 118, p. 111533, 2021.

- [17] Z. Mollaei, F. Kermani, F. Moosavi, S. Kargozar, J. V. Khakhi, and S. Mollazadeh, "In silico study and experimental evaluation of the solution combustion synthesized manganese oxide (MnO2) nanoparticles," *Ceramics International*, vol. 48, no. 2, pp. 1659-1672, 2022.
- [18] Y. Han, X. Wang, H. Dai, and S. Li, "Synthesis and luminescence of Eu3+ doped hydroxyapatite nanocrystallines: Effects of calcinations and Eu3+ content," *Journal of Luminescence*, vol. 135, pp. 281-287, 2013.
- [19] S. Park, J. Choi, V. H. M. Doan, and S. H. O, "Biodegradable manganese-doped hydroxyapatite antitumor adjuvant as a promising photo-therapeutic for cancer treatment," *Frontiers in Molecular Biosciences*, vol. 9, p. 1085458, 2022.
- [20] J. A. Ramos-Guivar, M. A. Morales, and F. J. Litterst, "γ-Fe2O3 nanoparticles embedded in nanohydroxyapatite matrix for magnetic hyperthermia and in vitro osteoblast cell studies," *Ceramics International*, vol. 46, no. 8, pp. 10658-10666, 2020.
- [21] S. P. Victor, W. Paul, V. Vineeth, R. Komeri, M. Jayabalan, and C. P. Sharma, "Neodymium doped hydroxyapatite theranostic nanoplatforms for colon specific drug delivery applications," *Colloids and Surfaces B: Biointerfaces*, vol. 145, pp. 539-547, 2016.
- [22] M. R. de Rezende *et al.*, "⁸⁹Sr-doped hydroxyapatite nanoparticles as a potential therapeutic agent for bone tumors," *International Journal of Applied Ceramic Technology,* vol. 16, no. 5, pp. 1904-1919, 2019.
- [23] F. Kermani *et al.*, "Iron (Fe)-doped mesoporous 45S5 bioactive glasses: Implications for cancer therapy," *Translational oncology*, vol. 20, p. 101397, 2022.
- [24] K. Sadeqzadeh *et al.*, "Electrospun nanofibers combined with Fe-doped mesoporous bioactive glass nanoparticles induce in vitro melanoma cell death," *Ceramics International, 50 (7), pp.* 11234-11245, 2024.
- [25] F. Gong *et al.*, "Tumor microenvironment-responsive intelligent nanoplatforms for cancer theranostics," *Nano Today*, vol. 32, p. 100851, 2020.
- [26] X. Wang, X. Zhong, Z. Liu, and L. Cheng, "Recent progress of chemodynamic therapy-induced combination cancer therapy," *Nano Today*, vol. 35, p. 100946, 2020.
- [27] H. Li *et al.*, "Lithium chloride suppresses colorectal cancer cell survival and proliferation through ROS/GSK-3β/NF-κB signaling pathway," *Oxidative medicine and cellular longevity*, vol. 2014, p. 241864, 2014.
- [28] A. Akhgari, D. A. GHALAMBOR, M. Rezaei, M. Kiarsi, and M. R. ABBASPOUR, "The design and evaluation of a fast-dissolving drug delivery system for loratadine using the electrospinning method," 2016.
- [29] P. G. Shikhi-Abadi and M. Irani, "A review on the applications of electrospun chitosan nanofibers for the cancer treatment," *International Journal of Biological Macromolecules*, vol. 183, pp. 790-810, 2021.
- [30] K. Azuma, T. Osaki, S. Minami, and Y. Okamoto, "Anticancer and anti-inflammatory properties of chitin and chitosan oligosaccharides," *Journal of functional biomaterials,* vol. 6, no. 1, pp. 33-49, 2015.
- [31] C.-L. Ke, F.-S. Deng, C.-Y. Chuang, and C.-H. Lin, "Antimicrobial actions and applications of chitosan," *Polymers*, vol. 13, no. 6, p. 904, 2021.
- [32] F. Avelelas *et al.*, "Antifungal and antioxidant properties of chitosan polymers obtained from nontraditional Polybius henslowii sources," *Marine drugs*, vol. 17, no. 4, p. 239, 2019.
- [33] P.-Y. Shih, Y.-T. Liao, Y.-K. Tseng, F.-S. Deng, and C.-H. Lin, "A potential antifungal effect of chitosan against Candida albicans is mediated via the inhibition of SAGA complex component expression and the subsequent alteration of cell surface integrity," *Frontiers in Microbiology*, vol. 10, p. 602, 2019.

- [34] S. Sarkar, D. Das, P. Dutta, J. Kalita, S. B. Wann, and P. Manna, "Chitosan: A promising therapeutic agent and effective drug delivery system in managing diabetes mellitus," *Carbohydrate polymers*, vol. 247, p. 116594, 2020.
- [35] A. A. D'souza and R. Shegokar, "Polyethylene glycol (PEG): a versatile polymer for pharmaceutical applications," *Expert opinion on drug delivery,* vol. 13, no. 9, pp. 1257-1275, 2016.
- [36] B. Qu and Y. Luo, "Chitosan-based hydrogel beads: Preparations, modifications and applications in food and agriculture sectors—A review," *International journal of biological macromolecules*, vol. 152, pp. 437-448, 2020.
- [37] T. Kokubo and H. Takadama, "How useful is SBF in predicting in vivo bone bioactivity?," *Biomaterials*, vol. 27, no. 15, pp. 2907-2915, 2006.
- [38] M. Salehi *et al.*, "Porous electrospun poly (ε-caprolactone)/gelatin nanofibrous mat containing cinnamon for wound healing application: In vitro and in vivo study," *Biomedical engineering letters*, vol. 10, pp. 149-161, 2020.
- [39] S. Nazarnezhad *et al.*, "Preparation and characterization of platelet lysate (PL)-loaded electrospun nanofibers for epidermal wound healing," *Journal of Pharmaceutical Sciences*, vol. 111, no. 9, pp. 2531-2539, 2022.
- T. E. Vaskivuo, F. Stenbäck, and J. S. Tapanainen, "Apoptosis and apoptosis-related factors Bcl-2, Bax, tumor necrosis factor-α, and NF-κB in human endometrial hyperplasia and carcinoma," *Cancer*, vol. 95, no. 7, pp. 1463-1471, 2002.
- [41] X. Dong *et al.*, "Synergistic combination of bioactive hydroxyapatite nanoparticles and the chemotherapeutic doxorubicin to overcome tumor multidrug resistance," *Small*, vol. 17, no. 18, p. 2007672, 2021.
- [42] B. Govindan *et al.*, "Designed synthesis of nanostructured magnetic hydroxyapatite based drug nanocarrier for anti-cancer drug delivery toward the treatment of human epidermoid carcinoma," *Nanomaterials*, vol. 7, no. 6, p. 138, 2017.
- [43] F. Kermani, A. Gharavian, S. Mollazadeh, S. Kargozar, A. Youssefi, and J. V. Khaki, "Silicon-doped calcium phosphates; the critical effect of synthesis routes on the biological performance,"

 Materials Science and Engineering: C, vol. 111, p. 110828, 2020.
- [44] Z. Mollaei, F. Kermani, S. Mollazadeh, S. Kargozar, and J. V. Khakhi, "Crystallization behavior and density functional theory study of solution combustion synthesized silicon doped calcium phosphates," *Ceramics International*, vol. 48, no. 10, pp. 14349-14359, 2022.
- [45] M. Kalbarczyk, A. Szcześ, A. Belcarz, P. Kazimierczak, and Z. May, "Zn-doped Mono- and Biphasic Calcium Phosphate Materials Derived from Agriculture Waste and Their Potential Biomedical Applications: Part I," *Materials*, vol. 16, no. 5, p. 1971, 2023.
- [46] H. Wang *et al.*, "Platelet membrane biomimetic bufalin-loaded hollow MnO2 nanoparticles for MRI-guided chemo-chemodynamic combined therapy of cancer," *Chemical Engineering Journal*, vol. 382, p. 122848, 2020.
- [47] R. Ramírez-Agudelo *et al.*, "Hybrid nanofibers based on polycaprolactone/gelatin/hydroxyapatite nanoparticles-loaded Doxycycline: Effective anti-tumoral and antibacterial activity," *Materials Science and Engineering: C,* vol. 83, pp. 25-34, 2018.
- [48] N. Salahuddin, E. M. Ibrahim, and M. El-Kemary, "Electrospun composite nanofibers based on PLA/Artesunate-loaded citrate-functionalized hydroxyapatite for boosting in vitro anticancer efficacy and drug delivery of artesunate," *Fibers and Polymers*, vol. 23, no. 12, pp. 3415-3426, 2022.
- [49] Z. Abedian *et al.*, "Anticancer properties of chitosan against osteosarcoma, breast cancer and cervical cancer cell lines," *Caspian journal of internal medicine*, vol. 10, no. 4, p. 439, 2019.

- [50] M. Raisova *et al.*, "The Bax/Bcl-2 ratio determines the susceptibility of human melanoma cells to CD95/Fas-mediated apoptosis," *Journal of investigative dermatology,* vol. 117, no. 2, pp. 333-340, 2001.
- [51] H. Zhao *et al.*, "Antitumor effect by hydroxyapatite nanospheres: Activation of mitochondria-dependent apoptosis and negative regulation of phosphatidylinositol-3-kinase/protein kinase B pathway," *ACS nano*, vol. 12, no. 8, pp. 7838-7854, 2018.
- [52] K. Xu *et al.*, "Anti-melanoma effect and action mechanism of a novel chitosan-based composite hydrogel containing hydroxyapatite nanoparticles," *Regenerative Biomaterials*, vol. 9, p. rbac050, 2022.
- [53] R. Wang *et al.*, "Anti-osteosarcoma effect of hydroxyapatite nanoparticles both in vitro and in vivo by downregulating the FAK/PI3K/Akt signaling pathway," *Biomaterials Science*, vol. 8, no. 16, pp. 4426-4437, 2020.
- [54] Z. Zhang, W. Yan, and Y. Ji, "A novel manganese dioxide-based drug delivery strategy via in situ coating γ-polyglutamic acid/cisplatin for intelligent anticancer therapy," *Journal of Materials Chemistry B*, vol. 11, no. 3, pp. 667-674, 2023.
- [55] Y.-S. Maeng, R. Lee, B. Lee, S.-i. Choi, and E. K. Kim, "Lithium inhibits tumor lymphangiogenesis and metastasis through the inhibition of TGFBIp expression in cancer cells," *Scientific reports*, vol. 6, no. 1, pp. 1-9, 2016.

Declaration of Competing Interest

The authors declare that they have no known competing financial interests or personal relationships that could have appeared to influence the work reported in this paper

Highlights

- Successful synthesis of manganese (Mn) and lithium (Li) doped calcium phosphates with specific properties.
- Fabrication of electrospun nanofibrous carriers using chitosan (CS) and polyethylene oxide (PEO) polymers.
- Demonstrated cytotoxicity on melanoma cells without affecting normal cells adversely.
- Significant induction of apoptosis in A375 cells shown through Annexin V/PI assay and qPCR analysis of apoptotic genes.